

# Fluctuations at Metal Halide Perovskite Grain Boundaries Create Transient Trap States: Machine Learning Assisted Ab Initio Analysis

Yifan Wu, Dongyu Liu, Weibin Chu, Bipeng Wang, Andrey S. Vasenko, and Oleg V. Prezhdo\*



Cite This: *ACS Appl. Mater. Interfaces* 2022, 14, 55753–55761



Read Online

ACCESS |

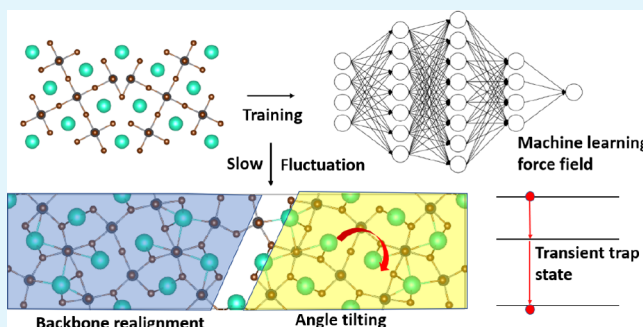
Metrics & More

Article Recommendations

Supporting Information

**ABSTRACT:** All-inorganic perovskites are promising candidates for solar energy and optoelectronic applications, despite their polycrystalline nature with a large density of grain boundaries (GBs) due to facile solution-processed fabrication. GBs exhibit complex atomistic structures undergoing slow rearrangements. By studying evolution of the  $\Sigma 5(210)$   $\text{CsPbBr}_3$  GB on a nanosecond time scale, comparable to charge carrier lifetimes, we demonstrate that GB deformations appear every  $\sim 100$  ps and increase significantly the probability of deep charge traps. However, the deep traps form only transiently for a few hundred femtoseconds. In contrast, shallow traps appear continuously at the GB. Shallow traps are localized in the GB layer, while deep traps are in a sublayer, which is still distorted from the pristine structure and can be jammed in unfavorable conformations. The GB electronic properties correlate with bond angles, with notable exception of the Br–Br distance, which provides a signature of halide migration along GBs. The transient nature of trap states and localization of electrons and holes at different parts of GBs indicate that charge carrier lifetimes should be long. At the same time, charge mobility can be reduced. The complex, multiscale evolution of geometric and electronic structures of GBs rationalize the contradictory statements made in the literature regarding both benign and detrimental roles of GBs in perovskite performance and provide new atomistic insights into perovskite properties.

**KEYWORDS:** all-inorganic  $\text{CsPbBr}_3$  perovskite, grain boundary, electron–hole recombination, charge traps, machine learning force field



## 1. INTRODUCTION

Lead halide perovskites are extensively investigated for optoelectronic and photovoltaic applications<sup>1–3</sup> due to facile and cheap solution-based fabrication process,<sup>1</sup> long electron–hole diffusion distances,<sup>4,5</sup> high charge carrier mobility,<sup>6</sup> high optical absorption,<sup>7</sup> and straightforward bandgap tuning,<sup>8,9</sup> which have led to the outstanding 25.5% power conversion efficiency of hybrid organic–inorganic perovskites (HOIPs).<sup>10</sup> Though the photovoltaic performance of the optimized HOIPs is already high, it is still below the Shockley–Queisser limit ( $\sim 33\%$ ),<sup>11</sup> and manipulation and control of charge traps can help approach the efficiency limit.<sup>12</sup> In addition, the instability of HOIPs in the presence of moisture, oxygen, and elevated temperature and the toxicity of lead stimulate research into all-inorganic halide perovskites, such as  $\text{CsPbX}_3$  ( $X = \text{Cl}, \text{Br}, \text{I}$ ), and non-lead perovskites, e.g.,  $\text{CsSnX}_3$  ( $X = \text{Cl}, \text{Br}, \text{I}$ ).<sup>13,14</sup> However, these alternative materials exhibit lower performance, providing strong motivation to study their defect properties. The structural stability of  $\text{CsPbX}_3$  and its outstanding intrinsic optoelectronic properties have allowed researchers to produce solar cells exceeding 20% efficiency,<sup>13</sup> motivating further studies of  $\text{CsPbX}_3$  perovskites.

Low-temperature thermal evaporation and solution-based processing of perovskite films inevitably introduce grain

boundary (GB) defects into pristine systems.<sup>15,16</sup> Although there are extensive studies of GBs in perovskites, understanding of the effect of GBs on charge trapping and recombination remains elusive due to the reported conflicting results. First-principles calculations indicate that GBs do not create midgap trap states and are electronically benign,<sup>7,17–19</sup> suggesting that GBs have a minor influence on the efficiency of the devices when the perovskite film morphology is homogeneous and compact.<sup>20</sup> In addition, researchers have reported that electron–hole recombination occurs mainly in nongrain boundary regions of the most studied  $\text{MAPbI}_3$  perovskite, indicating that GBs are benign to excited-state lifetime because GBs can only introduce shallow defects.<sup>21</sup> However, other experimental and theoretical results have defied such conclusions. Experimental studies have shown that the modification of grain size can notably influence the charge recombination rate and therefore impact the efficiency of solar

Received: September 8, 2022

Accepted: November 21, 2022

Published: December 7, 2022



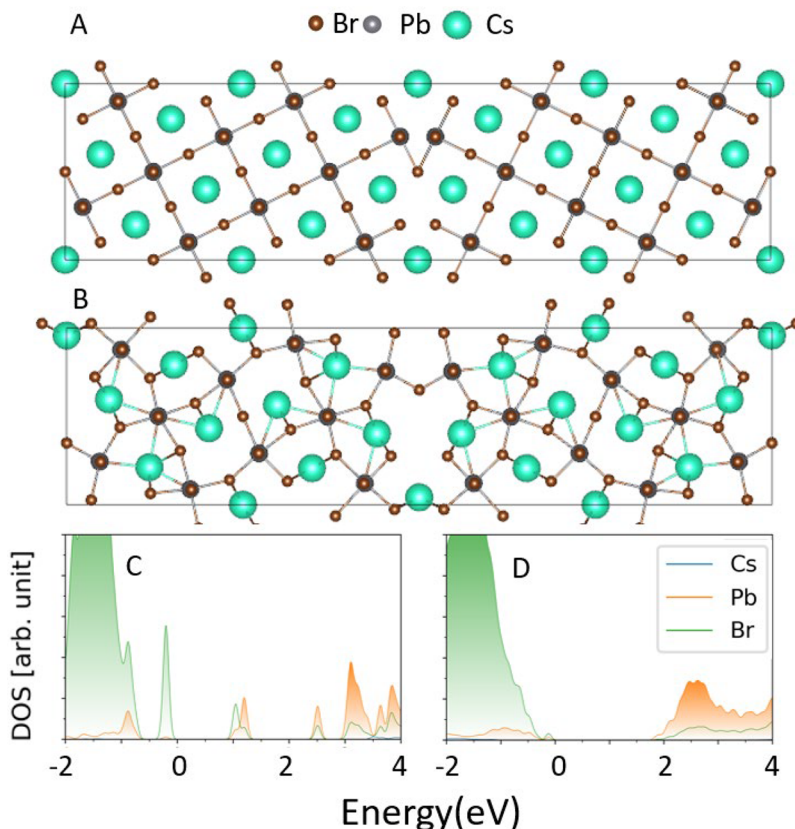


**Figure 1.** (A) Unoptimized  $\Sigma_5(210)$  grain boundary in  $\text{CsPbBr}_3$ . (B) Optimized grain boundary. (C) Density of states (DOS) of the unoptimized structure (corresponds to A) and (D) DOS of the optimized structure (corresponds to B). A significant structural relaxation occurs at the boundary, and all midgap states disappear after the optimization. Note that the system contains two equivalent grain boundaries due to periodic boundary conditions, in the middle and at the edges of the shown structures.

cells.<sup>22,23</sup> Tosun et al. have shown that the grain size can be increased by annealing and the annealed films exhibit much longer excited-state lifetimes.<sup>24</sup> Confocal fluorescence microscopy measurements, correlated to scanning electron microscopy, demonstrate photoluminescence quenching at GBs, indicating that GBs induce fast nonradioactive electron–hole recombination channels.<sup>25</sup> Theoretical studies have shown also that GBs can promote fast nonradiative charge recombination<sup>26,27</sup> due to high charge-trap densities at GBs.<sup>25,28</sup> Such contradictory conclusions, both experimental and theoretical, imply that the role of GBs in perovskite solar cells is quite complex, calling for more investigation and better understanding.

Most of the previous theoretical research on GBs has been based on short, few picosecond (ps) molecular dynamics (MD) trajectories or even just optimized structures due to computational limitations imposed by ab initio methodologies.<sup>7,17–19,26,27</sup> Recently, machine learning (ML) methods have gained immense popularity as promising tools to overcome the computational cost of ab initio methods to predict material properties<sup>29,30</sup> and structures,<sup>31</sup> construct ML force fields (FF),<sup>32</sup> and screen promising candidates for a variety of applications.<sup>33</sup> With the help of ML FFs generation of long MD trajectories with near ab initio accuracy is now feasible,<sup>34</sup> paving the way for studies of phenomena that occur over long time scales, such as anharmonic lattice dynamics,<sup>35</sup> phase transitions,<sup>36</sup> and chemical dynamics.<sup>37–40</sup> A ML FF modeling of perovskite GBs can capture the diversity of atomic configurations and their impact on the electronic structure.

Because charge carrier trapping and recombination occur on nanosecond (ns) time scales, ns trajectories are needed to elucidate the relevant GB properties in a comprehensive manner.

Motivated by the experimental works,<sup>22–25,28</sup> we develop a ML FF, investigate the atomistic evolution of geometric and electronic properties of the  $\Sigma_5(210)$  GB in the  $\text{CsPbBr}_3$  perovskite on a ns time scale comparable to the charge carrier lifetime, and analyze structure–property relationships using unsupervised ML. We demonstrate that regions with high likelihood of appearance of deep, midgap charge trap states appear at the GB due to structural fluctuations on a 100 ps time scale. However, the deep levels are transient and last only for a few hundred femtoseconds (fs). In contrast, shallow traps appear and disappear continuously along the 1.5 ns trajectory. Shallow traps are localized directly at the GB, while deep traps are in sub-GB layers, which can be jammed in unfavorable conformations. The properties of the states near the bandgap correlate with angles formed by atoms in the GB layer. They also correlate with the Br–Br distance, an indication of enhanced halide anion diffusion along GBs. The demonstrated multiscale evolution of the geometric and electronic properties of the  $\Sigma_5(210)$   $\text{CsPbBr}_3$  GB highlights the complex influence of GBs on perovskite performance. On the one hand, charge localization at GBs helps exciton separation, and the transient nature of trap states limits nonradiative carrier losses. On the other hand, charge localization at GBs reduces carrier mobility, and the low-density, dynamic GB region can facilitate ion migration and phase segregation.

## 2. METHODS

The geometry optimization, ab initio MD, density of states (DOS), and orbital spatial distribution calculations are performed with the Vienna ab initio Simulation Package.<sup>41</sup> The Perdew–Burke–Ernzerhof (PBE) exchange-correlation functional is used.<sup>42</sup> The interactions between electrons and ion cores are described by the projected-augmented wave method (PAW).<sup>43</sup> A simulation cell of 100 atoms is used to model the  $\Sigma 5(210)$  GB in  $\text{CsPbBr}_3$  (Figure 1). This GB has been studied previously.<sup>44,45</sup> Because perovskites are soft and are known to undergo large thermal fluctuations,<sup>38,46</sup> we expect that other grain boundaries should exhibit similar properties. The plane-wave basis energy cutoff is set to 350 eV for geometry optimization, electronic structure calculation, and ab initio molecular dynamics calculations. A  $3 \times 2 \times 1$   $k$ -point Monkhorst–Pack mesh is used for geometry optimization and electronic property characterization. Adiabatic MD is performed at the  $\Gamma$ -point only for computational efficiency because we are employing a relatively large simulation cell containing 20  $\text{CsPbBr}_3$  unit cells. The ML FF is built using the DeepMD package,<sup>32</sup> which uses deep learning and is capable of capturing the interatomic potential energy and forces based on a small amount of training data.

The geometry is optimized at 0 K. Then, the system is heated over a broad range of temperatures, from 100 to 1600 K at every 100 K, by velocity rescaling to obtain a diverse set of configurations in a canonical ensemble, serving as a training set for establishing the ML FF. Three thousand points are collected at 200, 300, and 400 K because the simulations focus on MD at room temperature, while 500 points are collected for the lower and higher temperatures to accomplish a broad screening of temperature–structure patterns. The collected data are used as input to feed the deep learning network embedded in the DeepMD. The model established in this way provides a good accuracy–efforts balance. Then, Lammmps<sup>47</sup> is used to carry out MD with the preobtained ML FF model. A 1.5 ns MD trajectory is obtained. The electronic properties of the system are studied every 50 ps along the 1.5 ns trajectory, and two 2 ps regions, at 700 and 850 ps, are investigated ab initio with a 2 fs time step. The potential energies from ab initio and ML FF calculations are compared to test the ML FF accuracy. In all cases, the root-mean-square error is around 10 meV per atom, as recommended.<sup>48</sup> The 2 ps region at 700 ps is analyzed further by computing mutual information (MI) between geometric features and electronic energy levels based on Sci-kit.<sup>49</sup> The structural information is generated with the modified symmetry function,<sup>50</sup> which is used to accurately capture the atom's radial and angular information in a specific chemical environment, while balancing the accuracy of description of structural details and the redundancy.<sup>51,52</sup> Various geometric features, such as bond angles and distances, are extracted as a time series from the MD trajectory. The extracted structural information is used to compute MI to analyze how the state energy level fluctuations depend on the geometric features of  $\text{CsPbBr}_3$ , because MI captures and quantifies the shared dependence of two variables.<sup>53–55</sup>

## 3. RESULTS AND DISCUSSION

To analyze the impact of the GB on the electronic structure of  $\text{CsPbBr}_3$ , we calculate the DOS of optimized and unoptimized structures, and the charge densities of the lowest unoccupied molecular orbital (LUMO) and the highest occupied molecular orbital (HOMO) for the optimized geometry. Figure 1 shows that the DOS is split into contributions from Cs, Pb, and Br atoms and that the unoptimized  $\Sigma 5(210)$  GB in  $\text{CsPbBr}_3$  introduces many shallow and deep trap states, which come from GB induced dangling and nonstoichiometric bonds.<sup>56</sup> The midgap trap states disappear after the geometry optimization, in agreement with the previous theoretical studies<sup>18,26</sup> demonstrating the capability of GB healing from trap states. The conduction band (CB) is primarily supported by Pb atoms, while the valence band (VB) originates primarily

from Br atoms, indicating that Cs atoms do not directly participate in the electron–hole recombination. The VB maximum (VBM) is identified as the antibonding hybridization between the Pb 6s and Br 4p orbitals, while the CB (CBM) minimum is supported by the Pb 6p and Br 4p orbitals.<sup>57</sup> Cs cations influence the charge carriers electrostatically and through mechanical interaction with the Pb–Br lattice. Our mutual information analysis (Table S1) also shows that angles, such as Cs–Pb–Cs and Cs–Br–Cs, with Pb and Br central atoms and involving Cs, have a relatively larger correlation with the state energy level fluctuations. These geometric features describe the deformation of the lattice structure. The DOS of the optimized  $\Sigma 5(210)$  GB shows a shallow trap state near the VBM that reduces the bandgap slightly, agreeing with the previous study.<sup>26</sup>

Figure 2 shows the HOMO and LUMO charge densities of the optimized  $\Sigma 5(210)$   $\text{CsPbBr}_3$  GB. The GB induces a

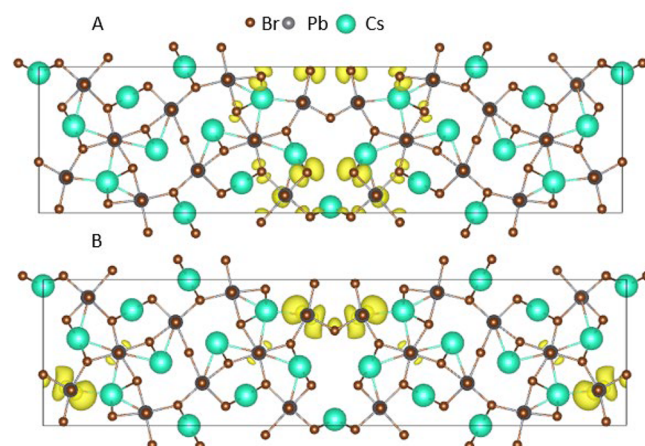


**Figure 2.** Charge densities of (A) HOMO and (B) LUMO in the optimized  $\Sigma 5(210)$  grain boundary structure. Although the states are strongly localized at the boundary, they are shallow traps (Figure 1D). The state energies are close to the corresponding bands, and the charges can easily escape into bands and undergo efficient long-range transport.

significant breaking of the periodic semiconductor symmetry. As a result, more phonon modes can couple to the electronic degrees of freedom,<sup>27,45</sup> and the charge densities show a strong localization in the GB regions for both the LUMO and the HOMO. GB defects inevitably introduce unsaturated and malformed chemical bonds, creating possibilities for fluctuations of atomic geometries in a long-run MD trajectory. Note that the simulation cell contains two GBs, in the middle and at the edges of the shown structures due to periodic boundary conditions used. Figures 2A,B show that the HOMO has a very strong contribution from the bromine atoms located in the central GB region. The LUMO arises from Pb–Pb atom pairs in the middle part and at the edges of the structure. Compared to the charge densities of pristine  $\text{CsPbBr}_3$ ,<sup>26</sup> grain boundary  $\text{CsPbBr}_3$  produces significant charge localization. The HOMO–LUMO overlap is decreased, and the nonadiabatic coupling responsible for nonradiative electron–hole recombination is reduced.<sup>45,58</sup>

When heated to 300 K, the  $\text{CsPbBr}_3$  GB shows significant distortions because of the perturbation to the optimal crystal structure and because lead halide perovskites are soft and can undergo slow large-scale motions around defects.<sup>38,46</sup> We

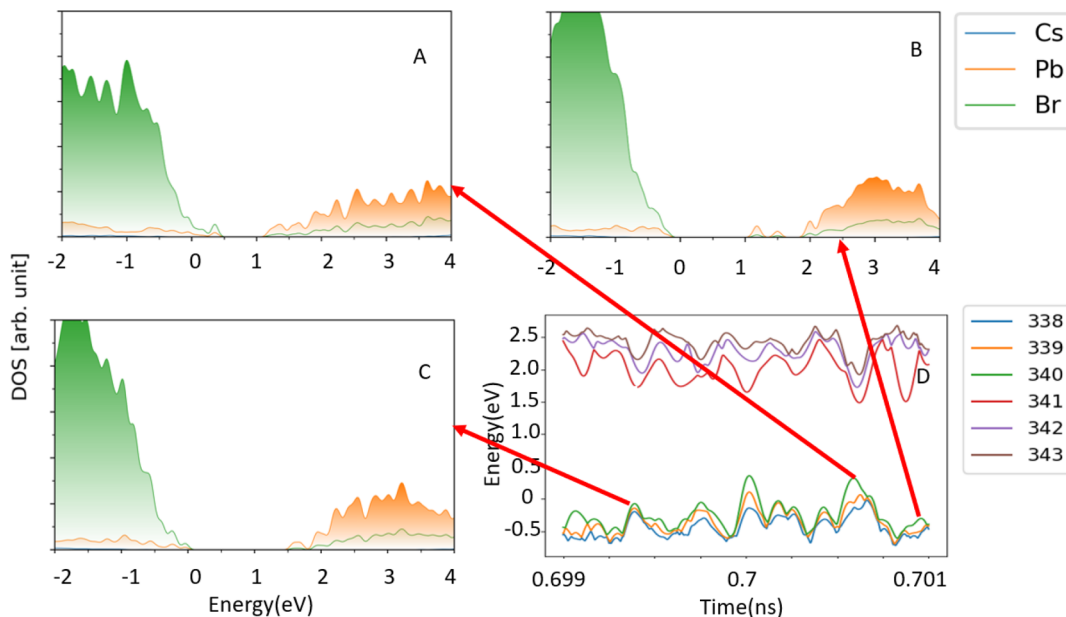


**Figure 3.** (A–C) Projected densities of states (DOS) at different points along a 2 ps part of the 1.5 ns trajectory (Figure S1). The zero energy is set at the valence band maximum. (D) Orbital energy levels along the 2 ps part of the 1.5 ns trajectory. The ab initio calculations are performed every 2 fs. The points in (D) are chosen from regions with good match between the machine learning and ab initio energies (Figure S2A). Trap states appear and disappear. Other examples are shown in Figure S3.

investigated ab initio electronic structure of the GB system every 50 ps along the 1.5 ns ML FF trajectory to grasp a general idea of the energy level fluctuations and the potential energy comparison (Figure S1). The ML FF slightly overestimates the potential energy, compared to the ab initio calculation; however, the fluctuations are reproduced well. The root-mean-square (RMS) error calculated for the whole 1.5 ns trajectory is 10.9 meV per atom, meeting the accuracy requirement.<sup>48</sup> A detailed comparison for two regions of the trajectory is shown in Figure S2. Training a ML FF for such a complex system as the GB is a challenging task, and the obtained accuracy is quite satisfactory. The total potential energy provides an overall estimate of the quality of the ML FF, and it is possible that forces on some atoms, especially those in the GB region, experience large deviations. To provide a more detailed test, we compare forces on individual atoms in the GB region (Figure S7) and away from the GB (Figure S8). The atom-by-atom comparison is favorable: The ML forces closely follow the ab initio forces. Slightly larger deviations are seen in the GB region, as should be expected. The GB region is essentially amorphous, and therefore it is impossible to expect the same ML FF quality as for small molecules with well-defined chemical bonding. To obtain ab initio data needed to sample such amorphous structures, we performed ab initio MD over a range of temperatures, reaching as high as 1600 K. At such high temperatures, significant distortions and fluctuations of the GB structure take place, leading to formation of transient deep traps. Transient traps are seen in the 1.5 ns ML FF trajectory at 300 K as well, but much less frequently.

Carrying out a standard ab initio MD calculation for 1.5 ns requires very significant investment of computational resources. For this reason, the previous theoretical studies focus on the optimized structure and a few picosecond trajectories of GB defects.<sup>18,26,27</sup> Such short-term simulations cannot capture the full diversity of atomic configurations that occur in a real system and can miss important slow fluctuations that influence

material properties. Both longer simulation time scales and larger systems are needed. The current work applies ML to extend the time scale by several orders of magnitude. Complementary approaches are being developed for increasing the system size.<sup>59,60</sup> The ML FF trajectory demonstrates that the GB undergoes a rapid, sub-10 ps sliding and tilting, which are followed by slower thermal fluctuations (Figure S5). The 31° tilt angle in the optimized structures increases to 45° by 30 ps and fluctuates around this value for the rest of the 1.5 ns trajectory. The screening of the energy level fluctuations along the 1.5 ns trajectory (Figure S1A) indicates a notable reduction of the gap between the HOMO (level 340) and the LUMO (level 341) on a 100 ps time scale. On some occasions the LUMO drops down in energy, while the HOMO remains close to the CBM. Often, the energy gap between the LUMO and the LUMO+1 (level 342) increases, indicating formation of transient midgap electron traps, separated energetically from the CB. The reduction of the HOMO–LUMO gap and the separation of the LUMO from the rest of the CB have a significant influence on charge carrier mobility and lifetime in the traditional semiconductors.<sup>61</sup> However, in the traditional semiconductors the trap states form stable configurations, allowing one to consider a static description of defect properties. In contrast, perovskites are much softer and undergo significant thermal structural fluctuations.<sup>38,46</sup> The midgap traps appear only transiently, as discussed in detail below, and should have much weaker influence on charge carrier dynamics.

To provide a more detailed analysis of the influence of long-time thermal fluctuations on the GB electronic structure, we chose two 2 ps regions at 700 ps (Figures 3–5) and 850 ps (Figures S3 and S4) of the 1.5 ns ML FF trajectory and investigated the electronic properties every 2 fs. The RMS errors in the potential energy between the ML FF and ab initio data are 11.79 and 8.60 meV per atom, and the evolution of the potential energies is given in Figure S2. The region around

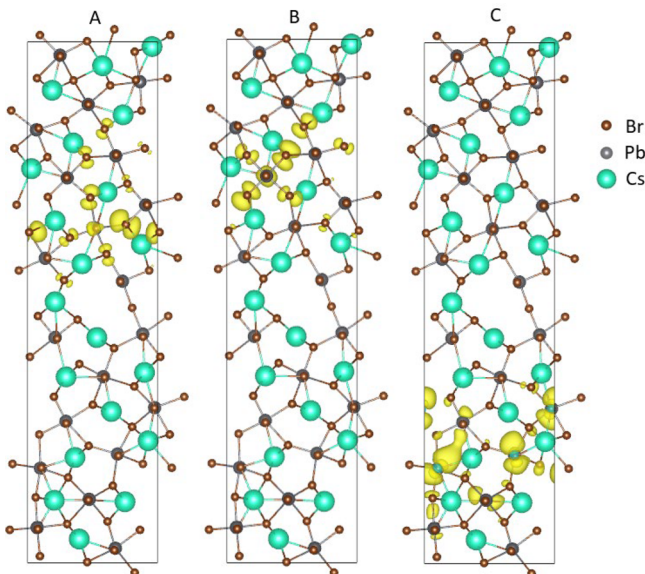


**Figure 4.** Charge densities of the trap states for the configuration shown in Figure 3A: (A) state 339, (B) state 340 (HOMO), and (C) state 341 (LUMO). The trap states are localized one or two layers away from the boundary. The boundary itself is sufficiently sparse and flexible to form the bonds needed to heal defects. The sub-boundary layers are distorted but cannot heal defects as well as the boundary itself. The hole trap shown in (B) is localized on a few Br atoms of the sub-boundary layer, in contrast to the hole trap of the optimized structure localized at the boundary (Figure 2A).

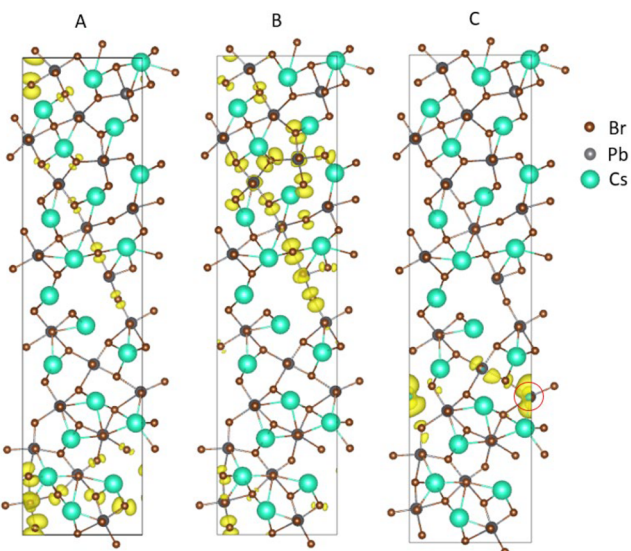


**Figure 5.** Charge densities of states for the configuration shown in Figure 3B: (A) state 339, (B) state 340 (HOMO), and (C) state 341 (LUMO). States 339 and 340 are HOMO-1 and HOMO and form the conduction band edge. They are more delocalized and contain contributions from grain boundary atoms. The deep electron trap state, LUMO, shown in (C) is localized around the circled Pb atom that has overly extended Pb–Br bonds (Figure S6A). The deep electron trap (C) is localized in the sub-boundary layer, similarly to the shall electron trap shown in Figure 4C.

700 ps exhibits a significant narrowing of the HOMO–LUMO energy gap, while the region around 850 ps does not show such narrowing (Figure S1A). We also report DOS and orbital charge densities at representative points.

The region around 700 ps demonstrates the emergence of both shallow and deep trap states (Figure 3), even though the optimized structure exhibits only a shallow hole trap (Figure 1D). A theoretical study was expecting midgap trap states in an optimized GB without additional point defects due to presence of dangling chemical bonds but did not report such states.<sup>18</sup> Thind et al. introduced a Br vacancy into the  $\Sigma(210)$  GB of  $\text{CsPbBr}_3$  and observed midgap trap states ascribed to Pb dangling bonds.<sup>61</sup> Even without deep traps, GBs have intrinsic dangling bonds that can facilitate ion migration<sup>62</sup> and significant geometry distortions. Sampling such behaviors requires long trajectories. Raising the energy of the occupied HOMO creates an energy penalty, however, the total potential energy fluctuates in a typical manner (Figure S2A) because the HOMO energy rise is offset by lowering of energy of other degrees of freedom. The emerging midgap states can serve as electron–hole recombination centers, promoting nonradiative decay, which could explain the detrimental nature of GBs reported by the experimental studies.<sup>25</sup> On the other hand, the deep trap states found in this and other examples are short-lived, lasting only a couple of hundred femtoseconds. The transient acceleration of the nonradiative electron–hole recombination at such instances is likely insufficient to make a large overall effect on the charge carrier lifetime, rationalizing the arguments that GBs are benign to the excited-state lifetime.<sup>21</sup> While sampling such fast transient appearance and disappearance of deep trap can be done directly at the ab initio level, the regions exhibiting such behavior appear on a hundreds of picoseconds time scale, which are hard to sample ab initio.

Figures 4 and 5 present charge densities of the frontier orbitals. Figure 4 corresponds to the DOS shown in Figure 3A. In this example, both HOMO and LUMO fluctuate deep into the bandgap and thus can be considered deep charge traps. Interestingly, these states are not localized at the GB. Rather, they are localized in the second layer near the GB. The GB itself exhibits a sparse distribution of atoms, allowing rearrangements needed to form missing chemical bonds and heal defects. In comparison, the second layer of the GB is much denser and compact, while it is still significantly distorted from perfect periodicity. The denser distorted second layer lacks the flexibility to heal from unsaturated or malformed bonds that cause the trap states. The HOMO–LUMO gap is reduced by about 1 eV in this example (Figure 3A) relative to the optimized GB structure (Figure 1D). However, such transient bandgap reduction lasts only 200 fs (Figure 3D). The charge densities shown in Figure 5 correspond to the DOS of Figure 3B. Here, only the LUMO drops deep into the bandgap, while the HOMO remains close to the VBM (Figure 3D). The deep trap LUMO is localized on the second GB layer (Figure 5C), while the HOMO–1 and HOMO are fairly delocalized and include bromines right at the GB (Figure 5A,B). Localization of HOMO and LUMO in different parts of the GB facilitates exciton dissociation and extends carrier lifetimes.<sup>45,58</sup>

We performed detailed electronic structure analysis for another time region at 850 ps, which does not exhibit very deep trap states (Figure S1A). The detailed energy level trajectory does show notable energy level fluctuations (Figure S3D) not seen in the coarse-grained trajectory (Figure S1A). However, these fluctuations are less significant than in the first example (cf. Figures 3D and S3D). Figure S3C demonstrates the disappearance of trap states, with the bandgap similar to

that of the optimized structure (Figure 1D), while Figure S3A,B shows the emergence of shallow traps near the CB. The examples of the electronic structure in different time regions suggest that geometric distortion and unsaturated chemical bonds in the GB region may or may not induce trap states and that trap states are very dynamic, appearing and disappearing from time to time, depending on the distortion.

To identify the key geometric features that correlate with fluctuations of the HOMO-1, HOMO, LUMO, and LUMO+1 energy levels, resulting in transient appearance of trap states, we computed MI between the energy levels and bond distance and angle geometric features—900 features in total. Such MI information analysis has been used previously to identify the key structural parameters responsible for non-radiative electron–hole recombination.<sup>53–55</sup> The top 5 most important features for each state are listed in Table S1. Overall, bond angles are more important than bond distances, indicating that the electronic properties couple more to structural distortions than bond breaking and formation. It is well established that the HOMO–LUMO gap in pristine perovskites depends strongly on tilting of  $\text{PbBr}_6$  octahedra,<sup>63</sup> and such tilting is described by corresponding bond angles. The conclusion remains true for the perovskite GB. The Pb–Br–Pb angle is most important for the LUMO, which gives rise to the deepest transient midgap state and which has been identified to play an important role in perovskite performance.<sup>57,64</sup>

The only bond distance features seen in Table S1 for HOMO and LUMO are Br–Br distances. Such bonds do not form in pristine perovskites, and transient formation of such bonds in the GB region is correlated to trap state formation. It has been proposed that Br and other halide anions exhibit enhanced migration along GBs, deteriorating perovskite performance and causing phase segregation and current–voltage hysteresis.<sup>65,66</sup> Transient formation of Br–Br bonds at the GB can be related to the Br migration.

To characterize the structural origin of the trap states, we calculated the bond lengths, angles, and coordination numbers for the atoms supporting the trap states. The analysis (Figure S6A,B) shows that the deep electron trap (Figure 5C) is localized on a few Pb atoms that lose coordination with the nearby Br atoms. Some of the Pb–Br bonds become very long, essentially broken. In comparison, the shallow electron trap (Figure 4C) is localized on multiple Pb atoms, whose angles with nearby bromines are significantly distorted from the optimal 180° value (Figure S6C,D). Note that the hole trap states seen in the MD trajectory are localized in sub-boundary layers (Figure 4B), while the hole trap in the optimized structure is localized directly at the GB (Figure 2A). The same observation holds for electron traps, indicating that optimized structures are not always characteristic of the material properties at a finite temperature.

The central atoms of the bond angles showing highest MI with the energy levels are highlighted by circles in Figure 6. As expected, atoms at the GB play the most important role. The majority of the features encountered in Table S1 are formed by Pb and Br atoms, which form the CB and VB electronic states. At the same time, many features contain Cs atoms as well, as seen in the prior analyses.<sup>67,68</sup> Although  $\text{Cs}^+$  cation do not contribute to the electronic states, they influence charge carriers electrostatically and through interactions with the surrounding  $\text{Br}^-$  anions.

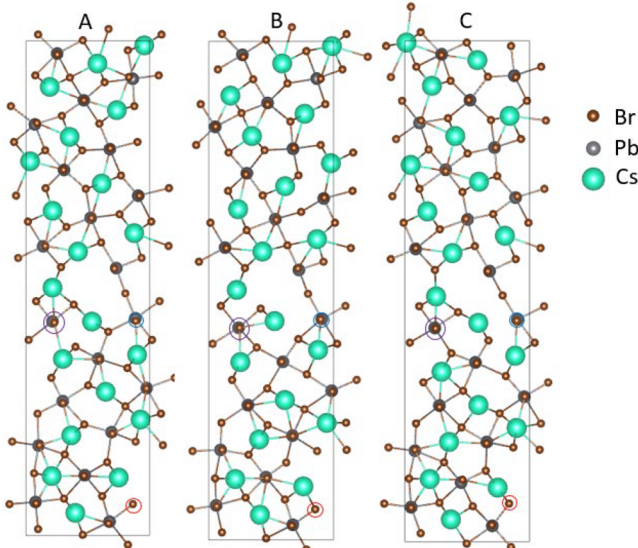


**Figure 6.** Geometric structures corresponding to the DOS shown in Figure 3. Parts A–C corresponds to parts A–C of Figure 3. Dangling bonds appear and disappear from time to time, giving rise to deep and shallow trap states and resulting in the reduced bandgap for some points along the trajectory. Geometric features of the marked atoms have high mutual information with the electronic energy levels (Table S1). The atoms are at the grain boundary and not sub-boundary, even though the deep trap states are localized in the sub-boundary (Figures 4 and 5) because most of the time the traps are not deep, and shallow traps are localized at the boundary (Figure 2). Note that the system has two grain boundaries, in the middle and top/bottom edges of the image, because of periodic boundary conditions.

The current analysis shows that the traps primarily split off the CB and are formed by under- or miscoordinated Pb atoms. To heal such electron traps, one can dope the systems with additional halides. There is experimental evidence that halide doping helps to reduce defect density,<sup>69,70</sup> and the current results suggest an atomistic explanation of this effect. More rarely, we observe hole trap states that split off the VB. These originate from miscoordinated Br atoms. If one attempts to heal electron traps by doping with halides, the density of trap states due to miscoordinated halides and halide interstitials can increase. Because electron traps are more frequent than hole traps, one can suggest moderate halide doping, such as to passivate the wrongly coordinated Pb atoms, while not to create too many halide interstitials.

The current study highlights the role slow structural fluctuation at perovskite GBs plays in governing GB electronic properties and demonstrates transient appearance midgap trap states for certain types of fluctuations. These transient trap states are different from trap states formed by structural defects, such as interstitials, vacancies, and substitutions. Earlier ab initio calculations have shown that point defects creating no or shallow traps in bulk perovskites can form deep and detrimental traps at GBs.<sup>71</sup> It is important to investigate the properties of such defects on longer time scales using ML FFs. The current conclusions are based on a 1.5 ns ML FF trajectory generated based on ab initio DFT training. The ML FF allowed us to sample GB conformations on the time scale comparable to the charge carrier lifetimes. Providing an important advance over the prior studies limited to a few picoseconds, the current model has limitations as well. GBs

exhibit a variety of bonding patterns, and development of a ML FF for such systems is quite challenging. The current ML model employed local descriptors, while more accurate models may be required based on global descriptors.<sup>72</sup> While the current simulation time is long, the GB size is quite small. Larger GB models can uncover other types of structures and motions. Such models can be obtained by application of ML techniques to parametrize electronic Hamiltonians.<sup>59,60</sup>

## 4. CONCLUSIONS

Based on ab initio DFT, we have developed a ML FF to describe structural evolution of the Σ5(210) GB in the CsPbBr<sub>3</sub> perovskite on the time scale comparable to the charge carrier lifetime. Then, we have investigated how slow structural changes at the GB influence the electronic structure. On a slow ~100 ps time scale we have observed fluctuations that give rise to regions with deep midgap trap states; however, the deep traps appear transiently for only a few hundred femtoseconds. In comparison, shallow traps appear and disappear constantly in the GB region. While shallow traps are localized in the GB layer, deep traps arise in a sublayer. The structure at the GB is sufficiently mobile to heal deep defects, while the sublayer structure is still distorted and can get stuck in unfavorable conformations generating deep midgap states. Both shallow and deep traps, as well as HOMO and LUMO that are energetically close to the VBM and CBM, are localized on just a few atoms. Such complex, multiscale behavior helps rationalize the contradictory statements made in the literature regarding both benign and detrimental influence of GBs on perovskite performance. The preponderance of shallow traps and the transient nature of deep traps indicate that these states do not create efficient charge recombination centers, and the HOMO and LUMO localization on different parts of the GB facilitates exciton dissociation and slows down charge recombination. At the same time, unfavorable distortions seen in the sublayer give rise to deep traps that can accelerate charge recombination, and significant localization of HOMO and LUMO can inhibit charge mobility.

The HOMO and LUMO properties correlate most with geometric features of atoms in the first GB layer. Bond angles correlate much more than bond distances because they determine tilts and distortions of PbBr<sub>6</sub> octahedra that govern perovskite electronic structure. Br–Br distance is a notable exception. It appears among the top features that correlate with the GB electronic properties and may be an indication of facile halide anion migration along GBs. Ion migration is detrimental to perovskite performance because it causes phase segregation and current–voltage hysteresis. Perovskite GBs are not necessarily stoichiometric and are often passivated. Therefore, it is important to conduct similar long-time MD studies of point defects at GBs and passivated GBs.<sup>27,71,73,74</sup> It is also important to study larger GB structures, other GBs, and GBs in different types of metal halide perovskites. The >1 ns atomistic analysis of fluctuations in the geometric and electronic properties provide important insights into the behavior of these unusual and highly efficient materials.

## ■ ASSOCIATED CONTENT

### SI Supporting Information

The Supporting Information is available free of charge at <https://pubs.acs.org/doi/10.1021/acsami.2c16203>.

Energy levels along the machine learning force field trajectory, distributions of bandgap and trap levels; comparison of potential energy and forces between machine learning and ab initio calculation; geometric structures, densities of states, charge densities for representative snapshots from another part of the 1.5 ns trajectory; schematic of structural evolution of the grain boundary; distributions of bond lengths and angles around trap states; mutual information scores between the top 5 features and frontier states (PDF)

## ■ AUTHOR INFORMATION

### Corresponding Author

Oleg V. Prezhdo – Department of Chemistry, University of Southern California, Los Angeles, California 90089, United States; Department of Physics and Astronomy, University of Southern California, Los Angeles, California 90089, United States;  [orcid.org/0000-0002-5140-7500](https://orcid.org/0000-0002-5140-7500); Email: [prezhdo@usc.edu](mailto:prezhdo@usc.edu)

### Authors

Yifan Wu – Department of Chemistry, University of Southern California, Los Angeles, California 90089, United States

Dongyu Liu – HSE University, 101000 Moscow, Russia;  [orcid.org/0000-0001-6941-1885](https://orcid.org/0000-0001-6941-1885)

Weibin Chu – Department of Chemistry, University of Southern California, Los Angeles, California 90089, United States; Key Laboratory of Computational Physical Sciences (Ministry of Education), Institute of Computational Physical Sciences, Fudan University, Shanghai 200433, China; Shanghai Qi Zhi Institute, Shanghai 200030, China;  [orcid.org/0000-0001-5951-0337](https://orcid.org/0000-0001-5951-0337)

Bipeng Wang – Department of Chemistry, University of Southern California, Los Angeles, California 90089, United States;  [orcid.org/0000-0003-0924-5867](https://orcid.org/0000-0003-0924-5867)

Andrey S. Vasenko – HSE University, 101000 Moscow, Russia; I.E. Tamm Department of Theoretical Physics, P.N. Lebedev Physical Institute, Russian Academy of Sciences, 119991 Moscow, Russia;  [orcid.org/0000-0002-2978-8650](https://orcid.org/0000-0002-2978-8650)

Complete contact information is available at: <https://pubs.acs.org/10.1021/acsami.2c16203>

### Notes

The authors declare no competing financial interest.

## ■ ACKNOWLEDGMENTS

The research was funded by the US National Science Foundation, Grant CHE-2154367. A.S.V. acknowledges support from the project 21-04-041 in the framework of the Academic Fund Program at HSE University in 2022.

## ■ REFERENCES

- (1) Bi, D.; Xu, B.; Gao, P.; Sun, L.; Grätzel, M.; Hagfeldt, A. Facile Synthesized Organic Hole Transporting Material for Perovskite Solar Cell with Efficiency of 19.8%. *Nano Energy* **2016**, *23*, 138–144.
- (2) Quarti, C.; De Angelis, F.; Beljonne, D. Influence of Surface Termination on the Energy Level Alignment at the Ch3nh3pbI3 Perovskite/C60 Interface. *Chem. Mater.* **2017**, *29*, 958–968.
- (3) Chen, Z.; Turedi, B.; Alsalloum, A. Y.; Yang, C.; Zheng, X.; Gereige, I.; AlSaggaf, A.; Mohammed, O. F.; Bakr, O. M. Single-Crystal MapbI3 Perovskite Solar Cells Exceeding 21% Power Conversion Efficiency. *ACS Energy Lett.* **2019**, *4*, 1258–1259.

- (4) Stranks, S. D.; Eperon, G. E.; Grancini, G.; Menelaou, C.; Alcocer, M. J.; Leijtens, T.; Herz, L. M.; Petrozza, A.; Snaith, H. J. Electron-Hole Diffusion Lengths Exceeding 1 Micrometer in an Organometal Trihalide Perovskite Absorber. *Science* **2013**, *342*, 341–344.
- (5) Gutiérrez Álvarez, S.; Lin, W.; Abdellah, M.; Meng, J.; Žídek, K.; Pullerits, T.; Zheng, K. Charge Carrier Diffusion Dynamics in Multisized Quaternary Alkylammonium-Capped  $\text{CspbBr}_3$  Perovskite Nanocrystal Solids. *ACS Appl. Mater. Interfaces* **2021**, *13*, 44742–44750.
- (6) Turren-Cruz, S.-H.; Saliba, M.; Mayer, M. T.; Juárez-Santiesteban, H.; Mathew, X.; Nienhaus, L.; Tress, W.; Erodić, M. P.; Sher, M.-J.; Bawendi, M. G.; et al. Enhanced Charge Carrier Mobility and Lifetime Suppress Hysteresis and Improve Efficiency in Planar Perovskite Solar Cells. *Energy Environ. Sci.* **2018**, *11*, 78–86.
- (7) Yin, W.-J.; Shi, T.; Yan, Y. Unique Properties of Halide Perovskites as Possible Origins of the Superior Solar Cell Performance. *Adv. Mater.* **2014**, *26*, 4653–4658.
- (8) Lao, X.; Li, X.; Ågren, H.; Chen, G. Highly Controllable Synthesis and Dft Calculations of Double/Triple-Halide  $\text{Cspbx}_3$  ( $X = \text{Cl}, \text{Br}, \text{I}$ ) Perovskite Quantum Dots: Application to Light-Emitting Diodes. *Nanomaterials* **2019**, *9*, 172.
- (9) Quarti, C.; Marchal, N.; Beljonne, D. Tuning the Optoelectronic Properties of Two-Dimensional Hybrid Perovskite Semiconductors with Alkyl Chain Spacers. *J. Phys. Chem. Lett.* **2018**, *9*, 3416–3424.
- (10) Yang, W. S.; Park, B.-W.; Jung, E. H.; Jeon, N. J.; Kim, Y. C.; Lee, D. U.; Shin, S. S.; Seo, J.; Kim, E. K.; Noh, J. H.; Seok, S., II Iodide Management in Formamidinium-Lead-Halide-Based Perovskite Layers for Efficient Solar Cells. *Science* **2017**, *356*, 1376–1379.
- (11) Shockley, W.; Queisser, H. J. Detailed Balance Limit of Efficiency of P-N Junction Solar Cells. *J. Appl. Phys.* **1961**, *32*, 510–519.
- (12) Jin, H.; Debroye, E.; Keshavarz, M.; Scheblykin, I. G.; Roeffaers, M. B.; Hofkens, J.; Steele, J. A. It's a Trap! On the Nature of Localised States and Charge Trapping in Lead Halide Perovskites. *Materials Horizons* **2020**, *7*, 397–410.
- (13) Gao, Y.; Wu, Y.; Lu, H.; Chen, C.; Liu, Y.; Bai, X.; Yang, L.; Yu, W. W.; Dai, Q.; Zhang, Y.  $\text{CspbBr}_3$  Perovskite Nanoparticles as Additive for Environmentally Stable Perovskite Solar Cells with 20.46% Efficiency. *Nano Energy* **2019**, *59*, 517–526.
- (14) Wu, Y.; Chu, W.; Vasenko, A. S.; Prezhdo, O. V. Common Defects Accelerate Charge Carrier Recombination in  $\text{CsSnI}_3$  without Creating Mid-Gap States. *J. Phys. Chem. Lett.* **2021**, *12*, 8699–8705.
- (15) Liu, Z.; Hu, J.; Jiao, H.; Li, L.; Zheng, G.; Chen, Y.; Huang, Y.; Zhang, Q.; Shen, C.; Chen, Q.; Zhou, H. Chemical Reduction of Intrinsic Defects in Thicker Heterojunction Planar Perovskite Solar Cells. *Adv. Mater.* **2017**, *29*, 1606774.
- (16) Wang, F.; Bai, S.; Tress, W.; Hagfeldt, A.; Gao, F. Defects Engineering for High-Performance Perovskite Solar Cells. *npj Flexible Electronics* **2018**, *2*, 1–14.
- (17) Yin, W.-J.; Chen, H.; Shi, T.; Wei, S.-H.; Yan, Y. Origin of High Electronic Quality in Structurally Disordered  $\text{Ch}_3\text{nh}_3\text{PbI}_3$  and the Passivation Effect of Cl and O at Grain Boundaries. *Adv. Electron. Mater.* **2015**, *1*, 1500044.
- (18) Guo, Y.; Wang, Q.; Saidi, W. A. Structural Stabilities and Electronic Properties of High-Angle Grain Boundaries in Perovskite Cesium Lead Halides. *J. Phys. Chem. C* **2017**, *121*, 1715–1722.
- (19) Thind, A. S.; Luo, G.; Hachtel, J. A.; Morrell, M. V.; Cho, S. B.; Borisevich, A. Y.; Idrobo, J. C.; Xing, Y.; Mishra, R. Atomic Structure and Electrical Activity of Grain Boundaries and Ruddlesden-Popper Faults in Cesium Lead Bromide Perovskite. *Adv. Mater.* **2019**, *31*, 1805047.
- (20) Castro-Méndez, A. F.; Hidalgo, J.; Correa-Baena, J. P. The Role of Grain Boundaries in Perovskite Solar Cells. *Adv. Energy Mater.* **2019**, *9*, 1901489.
- (21) Yang, M.; Zeng, Y.; Li, Z.; Kim, D. H.; Jiang, C.-S.; Van De Lagemaat, J.; Zhu, K. Do Grain Boundaries Dominate Non-Radiative Recombination in  $\text{Ch}_3\text{Nh}_3\text{PbI}_3$  Perovskite Thin Films? *Phys. Chem. Chem. Phys.* **2017**, *19*, 5043–5050.
- (22) Im, J.-H.; Jang, I.-H.; Pellet, N.; Grätzel, M.; Park, N.-G. Growth of  $\text{Ch}_3\text{nh}_3\text{PbI}_3$  Cuboids with Controlled Size for High-Efficiency Perovskite Solar Cells. *Nat. Nanotechnol.* **2014**, *9*, 927–932.
- (23) Ren, X.; Yang, Z.; Yang, D.; Zhang, X.; Cui, D.; Liu, Y.; Wei, Q.; Fan, H.; Liu, S. Modulating Crystal Grain Size and Optoelectronic Properties of Perovskite Films for Solar Cells by Reaction Temperature. *Nanoscale* **2016**, *8*, 3816–3822.
- (24) Tosun, B. S.; Hillhouse, H. W. Enhanced Carrier Lifetimes of Pure Iodide Hybrid Perovskite Via Vapor-Equilibrated Re-Growth (Verg). *Journal of physical chemistry letters* **2015**, *6*, 2503–2508.
- (25) de Quilettes, D. W.; Vorpahl, S. M.; Stranks, S. D.; Nagaoka, H.; Eperon, G. E.; Ziffer, M. E.; Snaith, H. J.; Ginger, D. S. Impact of Microstructure on Local Carrier Lifetime in Perovskite Solar Cells. *Science* **2015**, *348*, 683–686.
- (26) Wang, Y.; He, J.; Yang, Y.; Zhang, Z.; Long, R. Chlorine Passivation of Grain Boundary Suppresses Electron-Hole Recombination in  $\text{CspbBr}_3$  Perovskite by Nonadiabatic Molecular Dynamics Simulation. *ACS Appl. Energy Mater.* **2019**, *2*, 3419–3426.
- (27) Long, R.; Liu, J.; Prezhdo, O. V. Unravelling the Effects of Grain Boundary and Chemical Doping on Electron-Hole Recombination in  $\text{Ch}_3\text{nh}_3\text{PbI}_3$  Perovskite by Time-Domain Atomistic Simulation. *J. Am. Chem. Soc.* **2016**, *138*, 3884–3890.
- (28) Nie, W.; Tsai, H.; Asadpour, R.; Blancon, J.-C.; Neukirch, A. J.; Gupta, G.; Crochet, J. J.; Chhowalla, M.; Tretiak, S.; Alam, M. A.; Wang, H.-L.; Mohite, A. D. High-Efficiency Solution-Processed Perovskite Solar Cells with Millimeter-Scale Grains. *Science* **2015**, *347*, 522–525.
- (29) Liu, Z.; Wu, C. T.; Koishi, M. Transfer Learning of Deep Material Network for Seamless Structure-Property Predictions. *Computational Mechanics* **2019**, *64*, 451–465.
- (30) Wu, Y.; Prezhdo, N.; Chu, W. Increasing Efficiency of Nonadiabatic Molecular Dynamics by Hamiltonian Interpolation with Kernel Ridge Regression. *J. Phys. Chem. A* **2021**, *125*, 9191–9200.
- (31) Feng, S.; Zhou, H.; Dong, H. Application of Deep Transfer Learning to Predicting Crystal Structures of Inorganic Substances. *Comput. Mater. Sci.* **2021**, *195*, 110476.
- (32) Wang, H.; Zhang, L.; Han, J.; E, W. Deepmd-Kit: A Deep Learning Package for Many-Body Potential Energy Representation and Molecular Dynamics. *Comput. Phys. Commun.* **2018**, *228*, 178–184.
- (33) Rinderle, M.; Gagliardi, A. Machine Learning & Multiscale Simulations: Toward Fast Screening of Organic Semiconductor Materials. In *2021 International Conference on Numerical Simulation of Optoelectronic Devices (NUSOD)*, 2021; pp 1–2.
- (34) Smith, J. S.; Nebgen, B. T.; Zubatyuk, R.; Lubbers, N.; Devereux, C.; Barros, K.; Tretiak, S.; Isayev, O.; Roitberg, A. E. Approaching Coupled Cluster Accuracy with a General-Purpose Neural Network Potential through Transfer Learning. *Nat. Commun.* **2019**, *10*, 2903.
- (35) Lahnsteiner, J.; Bokdam, M. Anharmonic Lattice Dynamics in Large Thermodynamic Ensembles with Machine-Learning Force Fields: The Breakdown of the Phonon Quasiparticle Picture in  $\text{CspbBr}_3$ . *arXiv e-prints* **2021**, arXiv: 2101.06099.
- (36) Jinnouchi, R.; Lahnsteiner, J.; Karsai, F.; Kresse, G.; Bokdam, M. Phase Transitions of Hybrid Perovskites Simulated by Machine-Learning Force Fields Trained on the Fly with Bayesian Inference. *Phys. Rev. Lett.* **2019**, *122*, 225701.
- (37) Kulichenko, M.; Smith, J. S.; Nebgen, B.; Li, Y. W.; Fedik, N.; Boldyrev, A. I.; Lubbers, N.; Barros, K.; Tretiak, S. The Rise of Neural Networks for Materials and Chemical Dynamics. *J. Phys. Chem. Lett.* **2021**, *12*, 6227–6243.
- (38) Wang, B. P.; Chu, W. B.; Wu, Y. F.; Casanova, D.; Saidi, W. A.; Prezhdo, O. V. Electron-Volt Fluctuation of Defect Levels in Metal Halide Perovskites on a 100 Ps Time Scale. *J. Phys. Chem. Lett.* **2022**, *13*, 5946–5952.
- (39) Wang, B. P.; Chu, W. B.; Tkatchenko, A.; Prezhdo, O. V. Interpolating Nonadiabatic Molecular Dynamics Hamiltonian with Artificial Neural Networks. *J. Phys. Chem. Lett.* **2021**, *12*, 6070–6077.

- (40) Prezhdo, O. V. Modeling Non-Adiabatic Dynamics in Nanoscale and Condensed Matter Systems. *Acc. Chem. Res.* **2021**, *54*, 4239–4249.
- (41) Kresse, G.; Furthmüller, J. Efficient Iterative Schemes for Ab Initio Total-Energy Calculations Using a Plane-Wave Basis Set. *Phys. Rev. B* **1996**, *54*, 11169–11186.
- (42) Perdew, J. P.; Burke, K.; Ernzerhof, M. Generalized Gradient Approximation Made Simple. *Phys. Rev. Lett.* **1996**, *77*, 3865–3868.
- (43) Blöchl, P. E. Projector Augmented-Wave Method. *Phys. Rev. B* **1994**, *50*, 17953–17979.
- (44) Shan, W. T.; Saidi, W. A. Segregation of Native Defects to the Grain Boundaries in Methylammonium Lead Iodide Perovskite. *J. Phys. Chem. Lett.* **2017**, *8*, 5935–5942.
- (45) Wang, Y. T.; Fang, W. H.; Long, R.; Prezhdo, O. V. Symmetry Breaking at Mapbi(3) Perovskite Grain Boundaries Suppresses Charge Recombination: Time-Domain Ab Initio Analysis. *J. Phys. Chem. Lett.* **2019**, *10*, 1617–1623.
- (46) Chu, W. B.; Saidi, W. A.; Zhao, J.; Prezhdo, O. V. Soft Lattice and Defect Covalency Rationalize Tolerance of Beta-Cspbi3 Perovskite Solar Cells to Native Defects. *Angew. Chem., Int. Ed.* **2020**, *59*, 6435–6441.
- (47) Thompson, A. P.; Aktulga, H. M.; Berger, R.; Bolintineanu, D. S.; Brown, W. M.; Crozier, P. S.; in 't Veld, P. J.; Kohlmeier, A.; Moore, S. G.; Nguyen, T. D.; Shan, R.; Stevens, M. J.; Tranchida, J.; Trott, C.; Plimpton, S. J. Lammps - a Flexible Simulation Tool for Particle-Based Materials Modeling at the Atomic, Meso, and Continuum Scales. *Comput. Phys. Commun.* **2022**, *271*, 108171.
- (48) Wen, T.; Zhang, L.; Wang, H.; E, W.; Srolovitz, D. J. Deep Potentials for Materials Science. *Materials Futures* **2022**, *1*, 022601.
- (49) Pedregosa, F.; Varoquaux, G.; Gramfort, A.; Michel, V.; Thirion, B.; Grisel, O.; Blondel, M.; Prettenhofer, P.; Weiss, R.; Dubourg, V. Scikit-Learn: Machine Learning in Python. *Journal of Machine Learning Research* **2011**, *12*, 2825–2830.
- (50) Smith, J. S.; Isayev, O.; Roitberg, A. E. Ani-1: An Extensible Neural Network Potential with Dft Accuracy at Force Field Computational Cost. *Chemical science* **2017**, *8*, 3192–3203.
- (51) Behler, J.; Parrinello, M. Generalized Neural-Network Representation of High-Dimensional Potential-Energy Surfaces. *Phys. Rev. Lett.* **2007**, *98*, 146401.
- (52) Rupp, M.; Tkatchenko, A.; Müller, K.-R.; von Lilienfeld, O. A. Fast and Accurate Modeling of Molecular Atomization Energies with Machine Learning. *Phys. Rev. Lett.* **2012**, *108*, 058301.
- (53) Zhou, G.; Chu, W.; Prezhdo, O. V. Structural Deformation Controls Charge Losses in Mapbi3: Unsupervised Machine Learning of Nonadiabatic Molecular Dynamics. *ACS Energy Lett.* **2020**, *5*, 1930–1938.
- (54) Liu, D. Y.; Perez, C. M.; Vasenko, A. S.; Prezhdo, O. V. Ag-Bi Charge Redistribution Creates Deep Traps in Defective Cs2agpbbr6: Machine Learning Analysis of Density Functional Theory. *J. Phys. Chem. Lett.* **2022**, *13*, 3645–3651.
- (55) Mangan, S. M.; Zhou, G.; Chu, W.; Prezhdo, O. V. Dependence between Structural and Electronic Properties of Cspbi3: Unsupervised Machine Learning of Nonadiabatic Molecular Dynamics. *J. Phys. Chem. Lett.* **2021**, *12*, 8672–8678.
- (56) Yan, Y.; Jiang, C.-S.; Noufi, R.; Wei, S.-H.; Moutinho, H.; Al-Jassim, M. Electrically Benign Behavior of Grain Boundaries in Polycrystalline Cuinse 2 Films. *Physical review letters* **2007**, *99*, 235504.
- (57) Xiao, G.; Cao, Y.; Qi, G.; Wang, L.; Liu, C.; Ma, Z.; Yang, X.; Sui, Y.; Zheng, W.; Zou, B. Pressure Effects on Structure and Optical Properties in Cesium Lead Bromide Perovskite Nanocrystals. *J. Am. Chem. Soc.* **2017**, *139*, 10087–10094.
- (58) Shi, R.; Vasenko, A. S.; Long, R.; Prezhdo, O. V. Edge Influence on Charge Carrier Localization and Lifetime in Ch3nh3pbbr3 Perovskite: Ab Initio Quantum Dynamics Simulation. *J. Phys. Chem. Lett.* **2020**, *11*, 9100–9109.
- (59) Zubatiuk, T.; Nebgen, B.; Lubbers, N.; Smith, J. S.; Zubatyuk, R.; Zhou, G. Q.; Koh, C.; Barros, K.; Isayev, O.; Tretiak, S. Machine Learned Huckel Theory: Interfacing Physics and Deep Neural Networks. *J. Chem. Phys.* **2021**, *154*, 244108.
- (60) Pal, S.; Trivedi, D. J.; Akimov, A. V.; Aradi, B.; Frauenheim, T.; Prezhdo, O. V. Nonadiabatic Molecular Dynamics for Thousand Atom Systems: A Tight-Binding Approach toward Pyxaid. *J. Chem. Theory Comput.* **2016**, *12*, 1436–1448.
- (61) Thind, A. S.; Luo, G.; Hachtel, J. A.; Morrell, M. V.; Cho, S. B.; Borisevich, A. Y.; Idrobo, J.-C.; Xing, Y.; Mishra, R. Atomic Structure and Electrical Activity of Grain Boundaries and Ruddlesden-Popper Faults in Cesium Lead Bromide Perovskite. *Adv. Mater.* **2019**, *31*, 1805047.
- (62) Shao, Y.; Fang, Y.; Li, T.; Wang, Q.; Dong, Q.; Deng, Y.; Yuan, Y.; Wei, H.; Wang, M.; Gruverman, A.; Shield, J.; Huang, J. Grain Boundary Dominated Ion Migration in Polycrystalline Organic-Inorganic Halide Perovskite Films. *Energy Environ. Sci.* **2016**, *9*, 1752–1759.
- (63) Filip, M. R.; Eperon, G. E.; Snaith, H. J.; Giustino, F. Steric Engineering of Metal-Halide Perovskites with Tunable Optical Band Gaps. *Nat. Commun.* **2014**, *5*, 5757.
- (64) Huang, Y.; Yin, W.-J.; He, Y. Intrinsic Point Defects in Inorganic Cesium Lead Iodide Perovskite Cspbi3. *J. Phys. Chem. C* **2018**, *122*, 1345–1350.
- (65) Tong, C. J.; Cai, X. Y.; Zhu, A. Y.; Liu, L. M.; Prezhdo, O. V. How Hole Injection Accelerates Both Ion Migration and Nonradiative Recombination in Metal Halide Perovskites. *J. Am. Chem. Soc.* **2022**, *144*, 6604–6612.
- (66) Tong, C. J.; Geng, W.; Prezhdo, O. V.; Liu, L. M. Role of Methylammonium Orientation in Ion Diffusion and Current Voltage Hysteresis in the Ch3nh3pbbr3 Perovskite. *Acs Energy Letters* **2017**, *2*, 1997–2004.
- (67) How, W. B.; Wang, B. P.; Chu, W. B.; Kovalenko, S. M.; Tkatchenko, A.; Prezhdo, O. V. Dimensionality Reduction in Machine Learning for Nonadiabatic Molecular Dynamics: Effectiveness of Elemental Sublattices in Lead Halide Perovskites. *J. Chem. Phys.* **2022**, *156*, 054110.
- (68) How, W. B.; Wang, B.; Chu, W.; Tkatchenko, A.; Prezhdo, O. V. Significance of the Chemical Environment of an Element in Nonadiabatic Molecular Dynamics: Feature Selection and Dimensionality Reduction with Machine Learning. *J. Phys. Chem. Lett.* **2021**, *12*, 12026–12032.
- (69) Colella, S.; Mosconi, E.; Fedeli, P.; Listorti, A.; Gazza, F.; Orlandi, F.; Ferro, P.; Besagni, T.; Rizzo, A.; Calestani, G.; Gigli, G.; De Angelis, F.; Mosca, R. Mapbl(3-X) Cl-X Mixed Halide Perovskite for Hybrid Solar Cells: The Role of Chloride as Dopant on the Transport and Structural Properties. *Chem. Mater.* **2013**, *25*, 4613–4618.
- (70) Wang, T.; Jin, L. R.; Hidalgo, J.; Chu, W. B.; Snaider, J. M.; Deng, S. B.; Zhu, T.; Lai, B.; Prezhdo, O.; Correa-Baena, J. P.; Huang, L. B. Protecting Hot Carriers by Tuning Hybrid Perovskite Structures with Alkali Cations. *Science Advances* **2020**, *6*, eabb1336.
- (71) Qiao, L.; Fang, W. H.; Long, R.; Prezhdo, O. V. Atomic Model for Alkali Metal Passivation of Point Defects at Perovskite Grain Boundaries. *Acs Energy Letters* **2020**, *5*, 3813–3820.
- (72) Poltavsky, I.; Tkatchenko, A. Machine Learning Force Fields: Recent Advances and Remaining Challenges. *J. Phys. Chem. Lett.* **2021**, *12*, 6551–6564.
- (73) Qiao, L.; Fang, W. H.; Prezhdo, O. V.; Long, R. Suppressing Oxygen-Induced Deterioration of Metal Halide Perovskites by Alkaline Earth Metal Doping: A Quantum Dynamics Study. *J. Am. Chem. Soc.* **2022**, *144*, 5543–5551.
- (74) Shi, R.; Fang, W. H.; Vasenko, A. S.; Long, R.; Prezhdo, O. V. Efficient Passivation of Dy Center in Ch3nh3pbbr3 by Chlorine: Quantum Molecular Dynamics. *Nano Research* **2022**, *15*, 2112–2122.